IEEE Access
Multidisciplinary | Rapid Review | Open Access Journal

Received 13 July 2024, accepted 17 August 2024, date of publication 20 August 2024, date of current version 28 August 2024.

Digital Object Identifier 10.1109/ACCESS.2024.3446688

RESEARCH ARTICLE

Wearable Reconfigurable Antennas With Multi-Mode Switching for Sub-6GHz, V-Band, and D-Band Applications

MING-AN CHUNG, (Senior Member, IEEE), CHIA-WEI LIN, CHIH-WEI YANG, AND ING-PENG MEIY

Department of Electronic Engineering, National Taipei University of Technology, Taipei 10608, Taiwan

Corresponding author: Ming-An Chung (mingannchung@ntut.edu.tw)

This work was supported by the National Science and Technology Council, Taiwan, under Grant NSTC 113-2221-E-027-068.

ABSTRACT This paper proposes a wearable reconfigurable antenna which can be operated in sub-6GHz, V-band and D-band. In the sub-6GHz band, the dual loop antennas are combined with a diode switch to achieve multi-mode switching. In the V-band, a controllable beam from 0 to 360 degrees is achieved by using six combined Vivaldi antennas with a diode switch to switch between beam directions. The diamond-shaped monopole antenna designed for the D-band achieves extremely high transmission rates at close range and has upward-facing directional radiation. The antennas are available in the sub-6 GHz bands such as 2–2.4, 2.9–3, 4.3–4.7, 5.75–6.05, and 6.6–6.9 GHz. The antenna design in the V-band can cover 19.78% (41-50 GHz) of the fractional bandwidth with a reflection coefficient below the −10 dB standard. In the D-band diamond monopole antenna, the reflection coefficient can reach −10dB standard covering 16.25% (139.6–164.3GHz) of the fractional bandwidth, and with directional radiation, the maximum radiation can reach 12dBi.

INDEX TERMS Sub-6GHz, V-band, D-band, loop antenna, reconfigurable antenna, wideband antenna, PIN diode switches, multiband antennas.

I. INTRODUCTION

In recent years, the popularity of mobile communication applications in routine life shows that this technology is one of the most important areas [1]. To address this need, millimeter wave antennas are one of the solutions [2], as the demand for data transmission in wireless communication systems is increasing. Millimeter wave applications can be used in areas such as medical, industrial, scientific, and mobile communications, and to achieve information integration through the Internet of Things [3]. The key technologies required are equipment with different communication bands, controlled beam directionality and integrated sub-6 GHz and millimeter wave communication [4], [5], [6], [7], [8], [9].

To cover the demand of sub-6GHz and millimeter wave bands, it is made to have high gain and multi-band capability. The antennas in the sub-6 GHz and millimeter wave bands will be designed independently, and higher isolation will be achieved through different placement locations, as in [1] by placing the antennas in different bands separately to achieve 2.4, 5.2 and 60 GHz application bands. In [10], a multi-layer stacked antenna covering the sub-6 GHz and millimeter wave bands is proposed by designing three metal layers to achieve two antennas for S-band and Ka-band respectively. In [11], a curved monopole antenna for sub-6G GHz is designed in a mobile communication device and combined with a Patch antenna for millimeter wave to integrate dual-band antennas on the same structure.

To meet the objectives of multi-band [12], [13], [14], [15], [16], [17], beam switching [18], [19], [20], [21], [22], [23], [24], [25], and compactness, the most common approach is to design with reconfigurable antenna structures [26], [27], [28], [29], [30], [31], [32], [33], [34], [35], [36], [37], [38], [39], [40], [41], [42], such as the Fabry-Pérot (FP) cavity antenna proposed in [26], [27], and [28] for dual-band antenna designs. In [26], a dual-band aperture antenna is designed for

The associate editor coordinating the review of this manuscript and approving it for publication was Ali Karami Horestani.

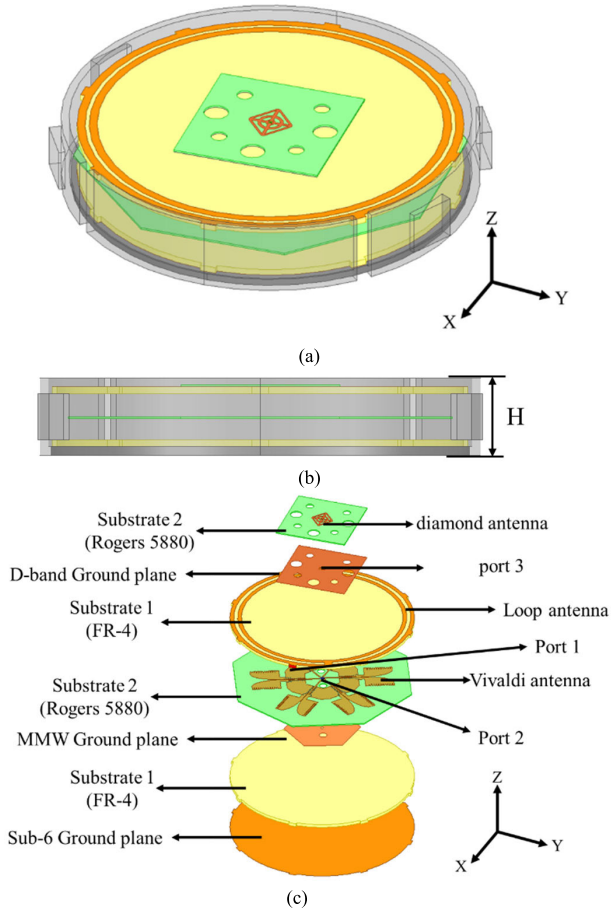

FIGURE 1. Geometry of the multi-frequency wearable reconstructed antenna. (a) 3D view. (b) Side view. (c) Exploded view. (H = 9mm).

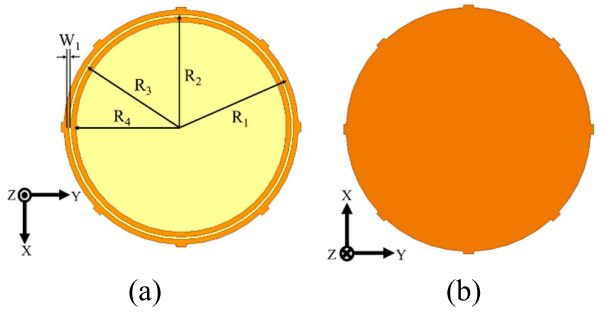

FIGURE 2. Double-layer loop antenna structure. (a) Top view. (b) Bottom view. $R_1 = 24$ mm, $R_2 = 24$ mm, $R_3 = 24$ mm, and $R_4 = 24$ mm.

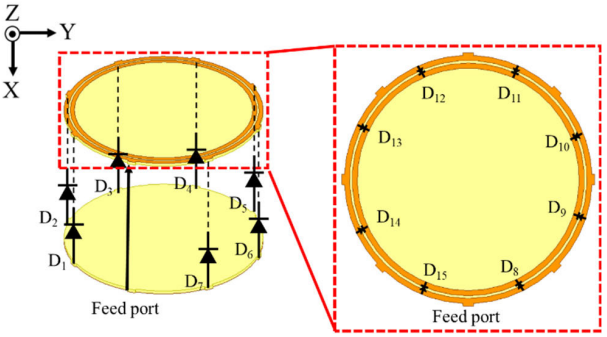

FIGURE 3. Height between baseboards and placement of diodes for Sub-6 band antennas.

X-band and Ka-band. The FP antenna is designed for X-band and the array antenna is designed for Ka-band, and the two antennas can be controlled independently for optimization and efficiency enhancement by sharing the aperture. In [27], a shared surface dual-band antenna design is proposed. The FP resonator is designed by substrate-integrated waveguide (SIW) and achieves a 10-dB fractional bandwidth of 23.45% (3.2-4.05 GHz) in S-band and 9.76% (26.8-29.55GHz) in Ka-band. In [29], [30], [43], [44], [45], and [46], MIMO techniques are used to design for more directional variations. As in [29], the 12 × 12 antenna design achieves 360° omni-directional radiation with good isolation. In [30], a tri-band shared antenna is introduced, which can achieve a common radiation aperture in three bands, and consists of an inverted-F antenna and a SIW leaky wave antenna. The overall gain can reach 12.29 dBi with ±36° beam coverage. In [31], a stack of patch antennas and SIW structures is proposed to achieve 7.3 dBi at low frequencies and 24 dBi at millimeter waves. In [32], the antenna gain in both bands is improved by sharing the radiation aperture. The literature [33] has designed an aperture sharing structure for 2.4, 5 and 60 GHz. It is mainly designed by stacked patch antennas at low frequencies and magneto-dipole antennas in the millimeter wave band, and can achieve good isolation. In [34], the proposed dual-band antenna consists of a four- cell structure and a dipole antenna, and reaches the operating bands of 3.5 GHz and 28 GHz.

In this paper, a multi-band wearable reconfiguration antenna is proposed for sub-6GHz, V-band and D-band applications. The sub-6GHz antenna is constructed by double-layer substrate on top and bottom, and the frequency band is switched by 15 diodes. The V-band antenna consists of six quasi-Vivaldi antennas between sub-6GHz substrates, with six diodes to switch at the feed end to control the beam direction. The D-band antenna is radiated from the top diamond antenna, allowing for high power transmission at close range.

II. GEOMETRY OF PROPOSED ANTENNA CONFIGURATION

Fig. 1 shows the multi-layer structure of the multi-band wearable reconfigured antenna. Two types of dielectric coefficient substrates are used in this structure, namely FR4 glass fiber substrate for sub-6GHz band with dielectric coefficient of 4.4, tangent loss of 0.02, and substrate thickness of 0.8mm. The V-band and D-band are based on Rogers 5880 substrates with a dielectric coefficient of 2.2 and a tangent loss of 0.0009. The Sub-6GHz antenna consists of two FR4 substrates stacked on top and bottom, the distance between the two substrates is 5.4mm, and the antenna structure consists of two ring antennas. The V-band antenna is placed in the middle of two FR4 substrates and the antenna consists of six quasi-Vivaldi

TABLE 1. Diode switches in 8 modes.

State	D_{15}	D_{14}	D_{13}	D_{12}	D_{11}	D_{10}	D_9	D_8	D_7	D_6	D_5	D_4	D_3	D_2	D_1
A	0	0	1	1	1	1	1	0	0	0	0	0	0	0	0
B	1	1	0	1	0	1	1	1	0	0	1	1	1	0	0
C	0	1	1	0	1	1	1	1	0	0	1	1	1	0	1
D	0	1	0	1	0	1	1	0	0	1	0	1	0	1	1
E	0	0	0	0	0	0	1	1	1	0	0	0	0	0	0
F	0	1	0	0	1	1	1	1	1	0	0	0	1	1	0
G	0	0	0	0	1	0	0	1	1	0	0	0	1	1	1
H	0	0	0	0	1	0	0	1	1	0	1	1	1	1	1

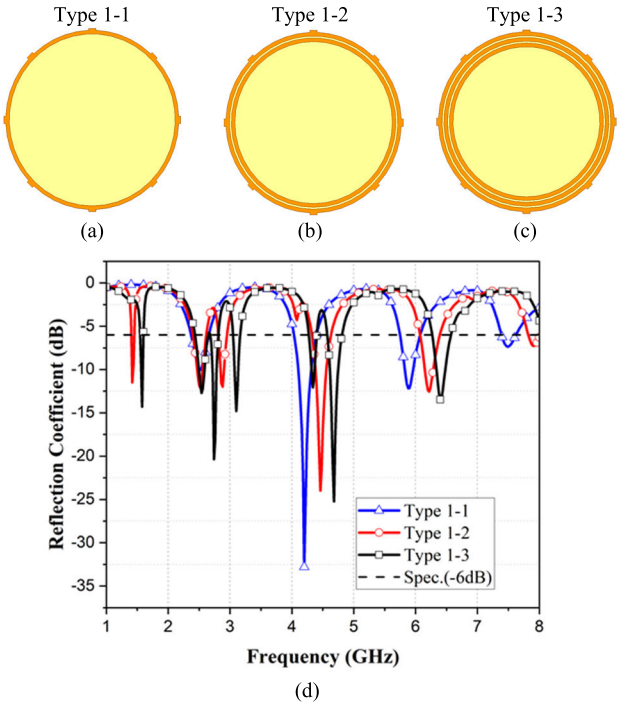

FIGURE 4. Antenna structure analysis. (a) Single-layer loop. (b) Dual-layer loops. (c) Triple-layer loops. (d) Reflection coefficient.

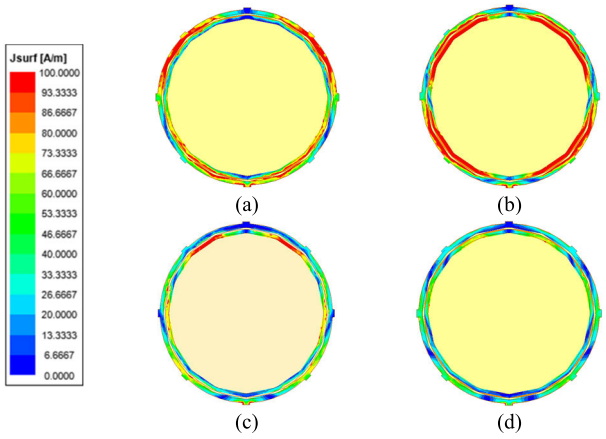

FIGURE 5. Current distribution of the dual loop antenna at (a) 2.52, (b) 2.88, (c) 4.46, and (d) 6.22 GHz.

antennas. The D-band antenna is bonded to the top FR4 substrate, and the antenna structure consists of a diamond-shaped antenna.

A. DUAL LOOP ANTENNA DESIGN FOR SUB-6 BAND

Fig. 2 shows the dual loop antenna structure for Sub-6GHz. Fig. 3 shows the relationship between the antenna and the diodes. The main structure consists of two loop antennas and is reconfigurable through seven controllable ground diodes and 8 diodes between the loops. Diodes D_1-D_7 can be sorted into 128 modes. These modes can be varied by changing the diodes D_8-D_{15} between the loop antennas to produce 256 controlled changes in each mode. Due to the symmetry of the antenna structure and the analysis of the applicable frequency bands by the simulation software, eight reflectance coefficient modes are finally listed for discussion, and the used modes and diode switches are organized in Table 1.

Fig. 4(a)-(c) shows the analysis of the three antenna structures, and Fig. 4(d) shows the reflection coefficient. In simulated reflection coefficients are shown for the −6 dB standard, covering 2.37-2.66, 4.03-4.4, and 5.75-6.07 GHz. Fig. 4(b) adds a second layer of loop structure, which will add a resonant frequency band at 2.81-2.95 GHz. In Fig. 4(c), when the loop structure is increased to the third layer, more resonant bands are generated under the −6dB standard, but the bandwidth performance is not great. The double-layer loop structure has the best resonant band, and it is finally chosen as the final design. Fig. 5 shows the current distribution of the dual loop antenna at each frequency band. Fig. 5(a) shows the current distribution at 2.52 GHz, and the current is concentrated at 60 degrees and 330 degrees of the peripheral loop antenna. The 2.82GHz current in Fig. 5(b) is mainly distributed between the two loops at 60, 120, 210 and 330 degrees. At 4.46GHz, the currents are concentrated at 60 and 330 degrees of the inner loop antenna, as shown in Figure 5(c). Fig. 5(d) shows that the current at 6.22GHz is equally distributed among the loop antennas.

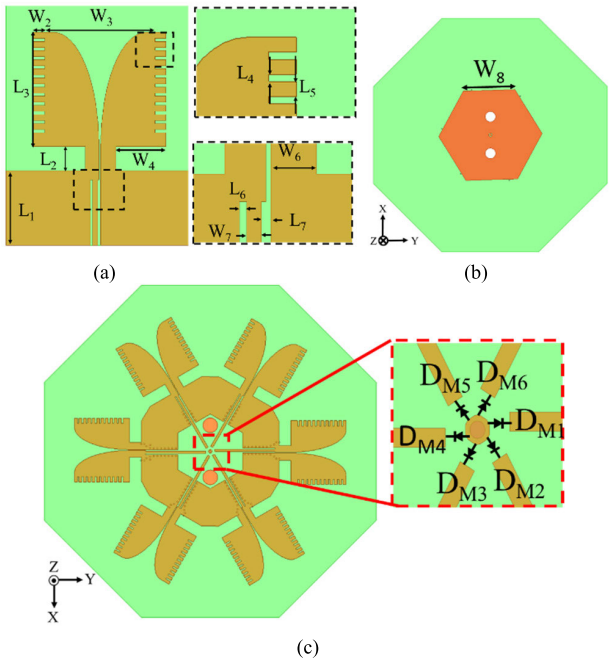

FIGURE 6. Detailed structure of the V-band antenna. (a) Dimensions of the front of the antenna. (b) Ground structure. (c) Diode distribution. ($L_1 = 4.9$mm, $L_2 = 1.6$mm, $L_3 = 7.5$mm, $L_4 = 0.2$mm, $L_5 = 0.4$mm, $L_6 = 0.15$mm, $L_7 = 0.2$mm, $L_8 = 0.4$mm, $W_2 = 0.725$mm, $W_3 = 7.25$mm, $W_{24} = 3.3$mm, $W_5 = 7.25$mm, $W_6 = 1$mm, $W_7 = 0.325$mm, $W_8 = 10$mm).

TABLE 2. Diode switches in 8 modes.

State	D_{M6}	D_{M5}	D_{M4}	D_{M3}	D_{M2}	D_{M1}
1	0	0	0	0	0	1
2	0	0	0	0	1	1
3	0	0	0	1	0	1
4	0	0	1	0	0	1
5	0	0	0	1	1	1
6	0	0	1	0	1	1
7	0	1	0	1	0	1
8	0	0	1	1	1	1
9	0	1	0	1	1	1
10	0	1	1	1	1	1

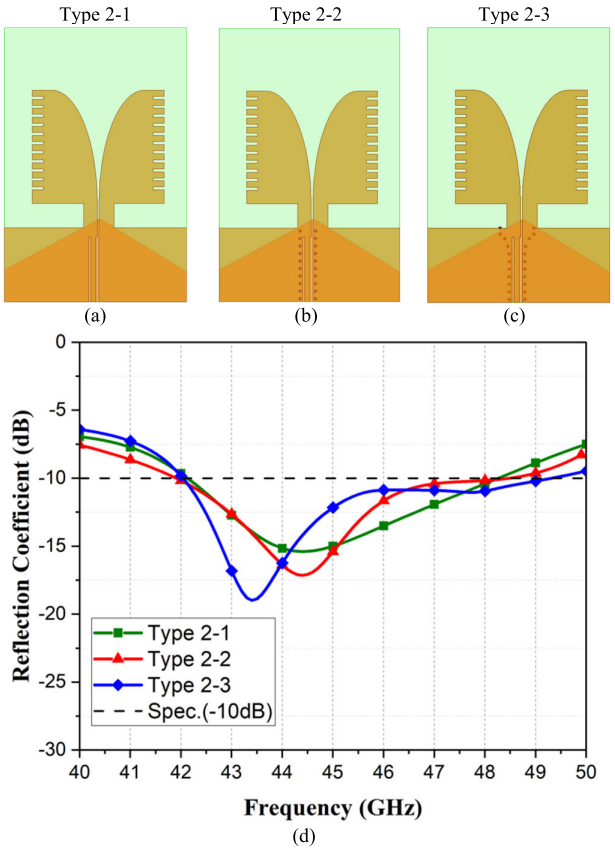

FIGURE 7. Analysis of the antenna GCPW structure. (a) CPW structure. (b) GCPW structure. (a) Quasi-GCPW structure. (d) Reflection coefficient.

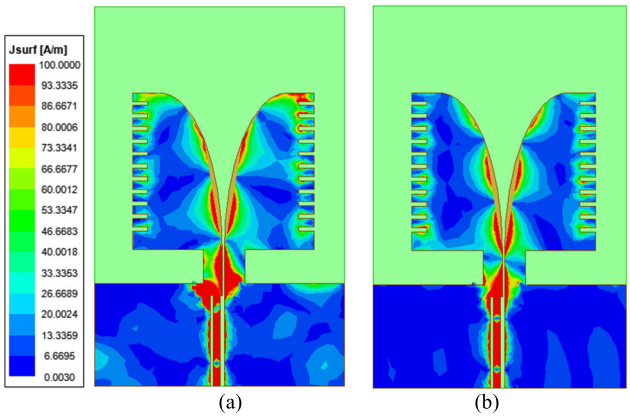

FIGURE 8. Vivaldi antenna current distribution at (a) 43.4 and (b) 47 GHz.

B. VIVALDI ANTENNA DESIGN FOR THE V-BAND

Fig. 6(a) and (b) show the designed reconfigurable V-band antenna top view and ground plane, and the diode distribution as in Fig. 6(c). The antenna structure consists of six identical quasi-Vivaldi antennas with six diode switches at the feed point to switch the current flow, allowing for 360 degree-controlled beam-switching and the ability to turn on the required diodes simultaneously to obtain the desired beam direction. The back of the antenna is made up of a hexagonal patch with an internal pin at the center of the feeding end, which transmits the feeding signal to the antenna. Table 2 shows all the listed modes, which can be divided into 11 different modes due to the symmetric structure.

Fig. 7 shows the effect of the grounded coplanar waveguide (GCPW) structure on the reflection coefficient. In Fig. 7(a), no GCPW exists between the ground plane and the transmission line, and the reflection coefficients can be seen to be higher than −10 dB. In Fig. 7(b), the coplanar waveguide

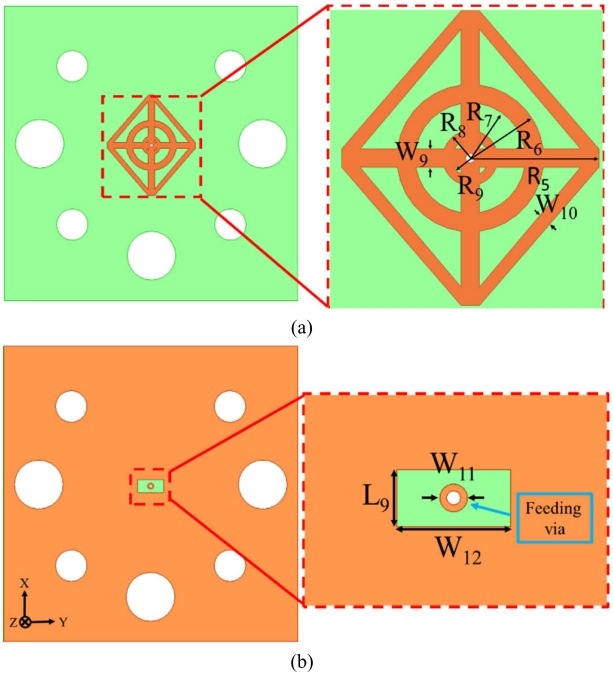

FIGURE 9. Detailed dimensions of the D-band diamond-shaped monopole antenna structure. (a) Antenna structure. (b) Detailed dimensions of the feed-in structure. ($L_9 = 0.855$mm, $W_9 = 0.4$mm, $W_{10} = 0.2$mm, $W_{11} = 0.4$mm, $W_{12} = 1.651$mm, $R_5 = 2.8$mm, $R_6 = 1.6$mm, $R_7 = 1.2$mm, $R_8 = 0.6$mm, $R_4 = 0.4$mm).

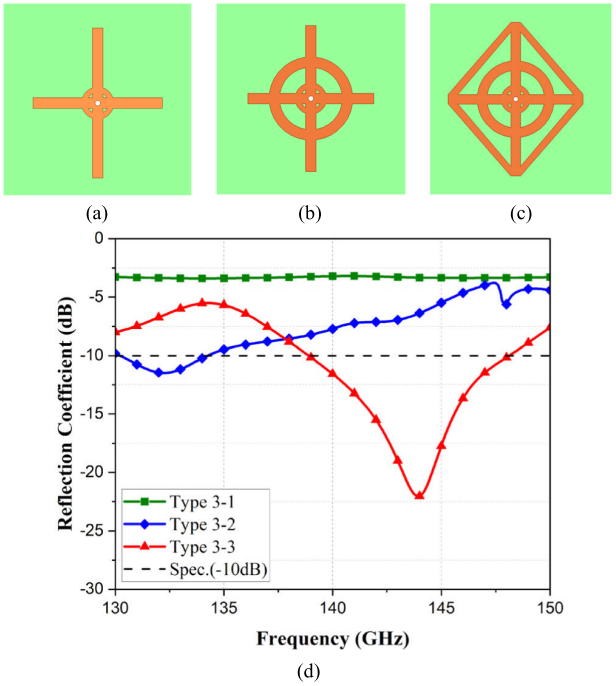

FIGURE 10. (a) Evolution of D-band monopole rhombus structure. (b) Reflection coefficient.

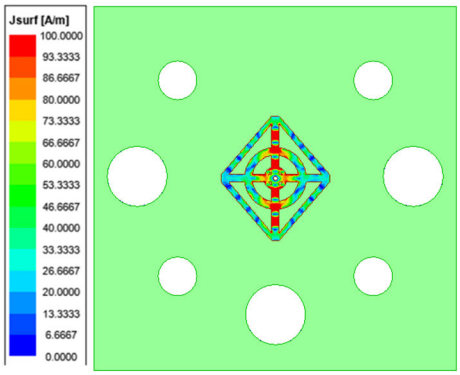

FIGURE 11. Current distribution of diamond-shaped monopole antenna at 144 GHz.

(CPW) structure is added between the transmission lines, and the result shows that the reflection coefficient is resonant at high frequencies, but the reflection coefficient is higher than −10 dB as in Type 2-1. In Fig. 7(c), the GCPW structure near the antenna is modified so that the shape is close to the Y-shaped structure, and the best bandwidth of 42-50 GHz can be achieved in Type 2-3. Fig. 8 depicts the current distribution of the Vivaldi antenna at 43.4 and 47 GHz. The current at 43.4 GHz is concentrated in the GCPW structure and at the top of the Vivaldi antenna, and there is a slight leakage of current at ground level. At 47 GHz, the current distribution is concentrated in the center of the Vivaldi antenna, and there is less current leakage at ground level.

C. D-BAND MONOPOLE ANTENNA

Fig. 9(a) shows the structure of the front of the diamond antenna, which is composed of two rings of progressively increasing diameter and surrounded by a diamond ring at the outermost circumference. Fig. 9(b) shows a 1.651mm × 0.8255mm rectangular slot etched into the center of the ground plane. A 0.4mm diameter via was added in the center of the rectangular slot. To simulate the real environment, only the thin copper shell was removed from the center of the via. Fig. 10(a)-(c) shows the evolution of the antenna, and Fig. 10(d) shows the change of reflection coefficient. As shown in Fig. 10(a), the antenna structure consisting of a cross, and a center ring does not resonate at a reflection coefficient of −10 dB. In Fig. 10(b), adding a second circular ring to the antenna, a bandwidth of 130-134.2 GHz can be seen at the −10 dB standard, but only about −12 dB at the deepest point of resonance, which shows a poor matching effect. In Fig. 10(c), the Type3-3 of the outermost diamond ring structure is added so that the bandwidth at −10dB standard can reach the bandwidth of 138.9-148GHz and the deepest −22dB resonance depth at 144GHz. The current distribution of the rectangular monopole antenna at 146 GHz is shown in Fig. 11, and the maximum current is concentrated in the cross structure from 0 degrees to 180 degrees and spreads to both sides of the structure.

D. ANALYSIS OF HAND EFFECT

Fig. 12 shows the performance of the sub-6 GHz, V- and D-Band antennas in hand and free space. From Fig. 12(a)-(c),

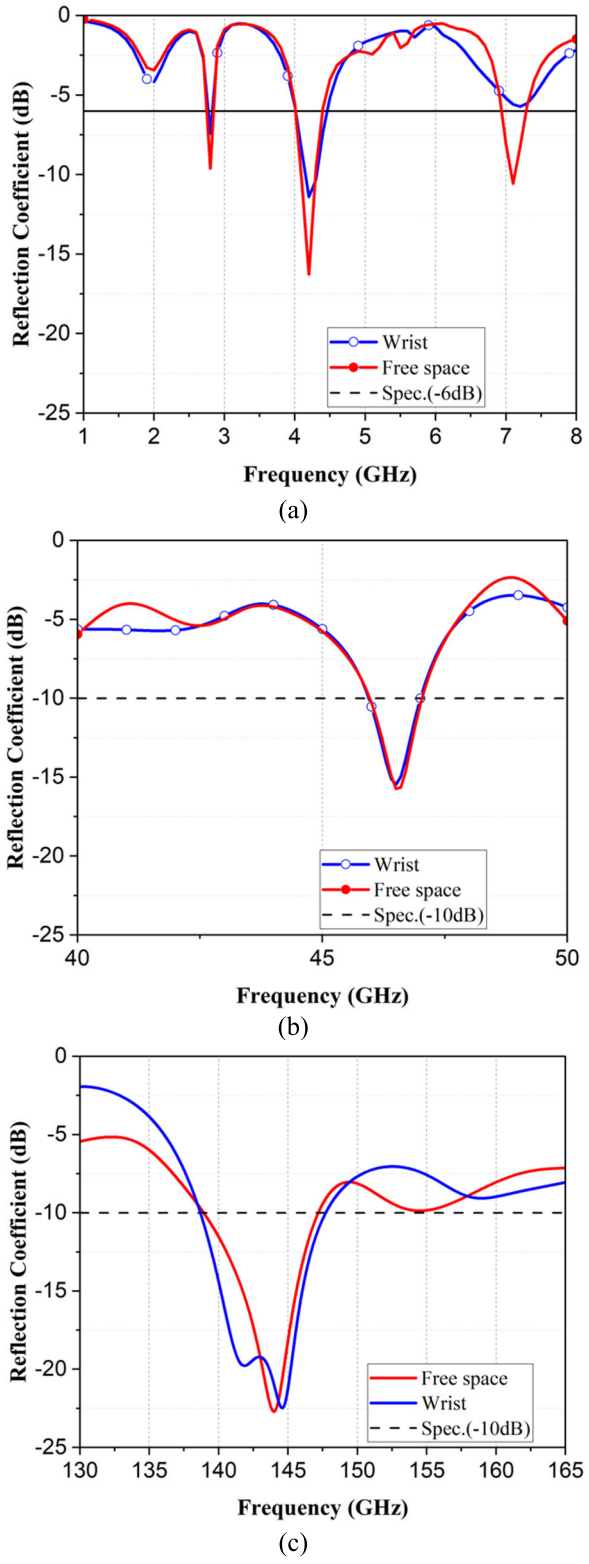

FIGURE 12. Hand effect of (a) Sub-6 GHz, (b) V-, and (c) D-Band antennas.

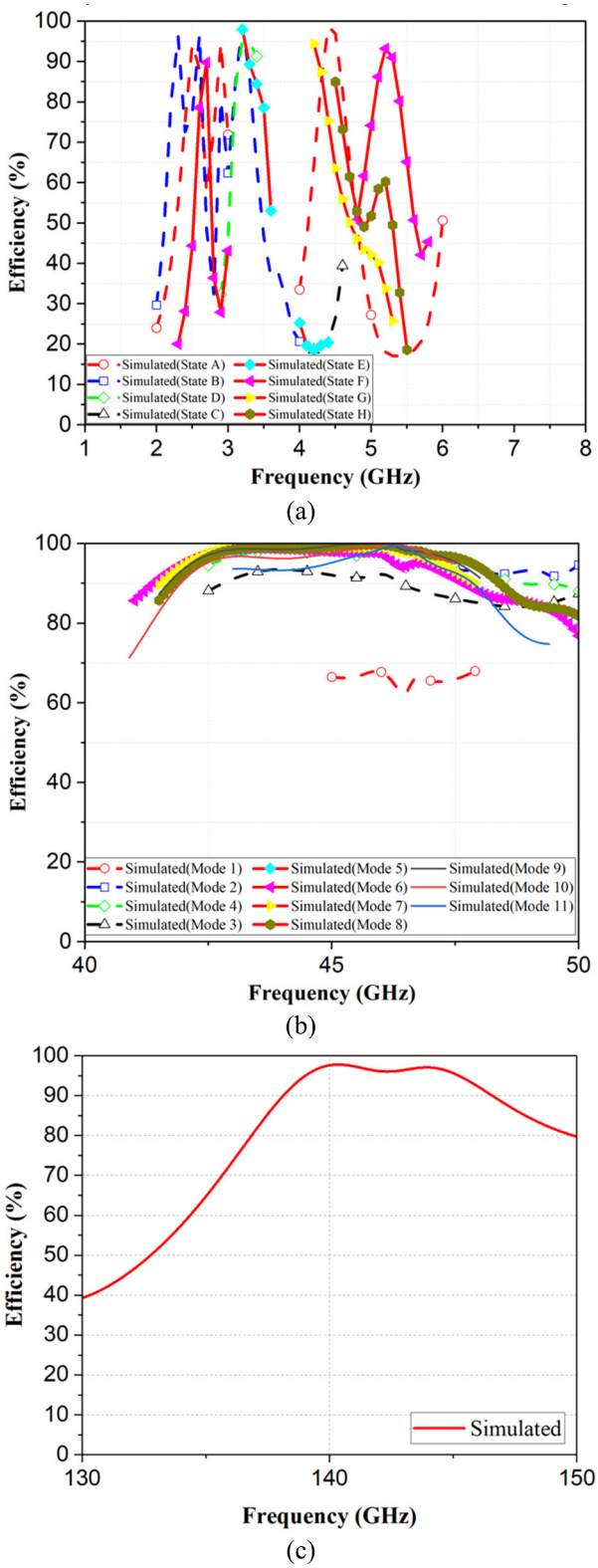

FIGURE 13. Radiation efficiency of (a) Sub-6 GHz, (b) V-, and (c) D-Band antennas.

the reflection coefficients of the sub 6GHz antenna are similar in the wrist and free space, and the V- and D-Band antennas also have the same results with the sub 6GHz. Therefore, the structure of the sub 6GHz, V- and D-Band antennas is not affected drastically by being worn on the wrist.

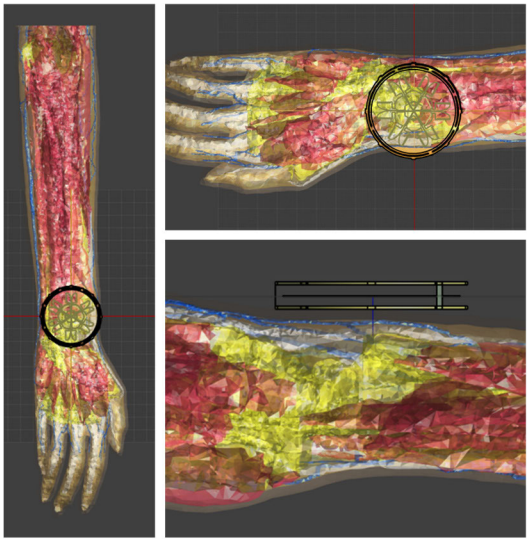

FIGURE 14. Antenna structure configuration on Sim4life simulation software.

E. ANALYSIS OF RADIATION EFFICIENCY

Fig. 13 shows the radiation efficiency of sub-6 GHz, millimeter wave and D-Band antennas. The radiation efficiency of sub-6 GHz antennas is in the range of 84.9-98.6%. The millimeter-wave antennas have radiated efficiencies in 67.9-99.9%, and the D-Band antennas have radiated efficiencies of 95.6%.

III. BODY RADIATION EFFECTS

The effects of antenna radiation on the human body need to be evaluated if the antenna is used in a wearable device. Excessive or prolonged absorption of radiation may cause damage to human body tissues. Therefore, wearable devices are required to meet the international or local standards of electromagnetic energy absorption ratio (Specific Absorption Rate, SAR) [47], which indicates the ratio of radio frequency power absorption rate per unit mass of tissue per unit time. The commonly used SAR value range includes 10 kHz to 10 GHz, and the SAR value calculation is expressed by (1).

$$SAR = \frac{\sigma \cdot |E|^2}{\rho_m} \tag{1}$$

where σ is the human conductivity, E is the electric field in the tissue, and ρ_m is the mass density of the tissue.

The SAR values and distributions evaluated in this paper are based on the Federal Communications Commission (FCC) standard of not exceeding 1.6 W/kg per 1 gram of tissue on average. Fig. 14 shows the antenna placed on top of the hand model. The distribution of SAR values for the eight modes is shown in Fig. 15. The designed antenna can be seen to be below the standard of 1.6 W/kg for 1 gram of tissue, which is well suited for wearable applications.

The next step is the effect of millimeter wave antennas on the human body. The time-averaged power($\vec{S}$) in the millimeter wave band is analyzed by (2), where Re is denoted as

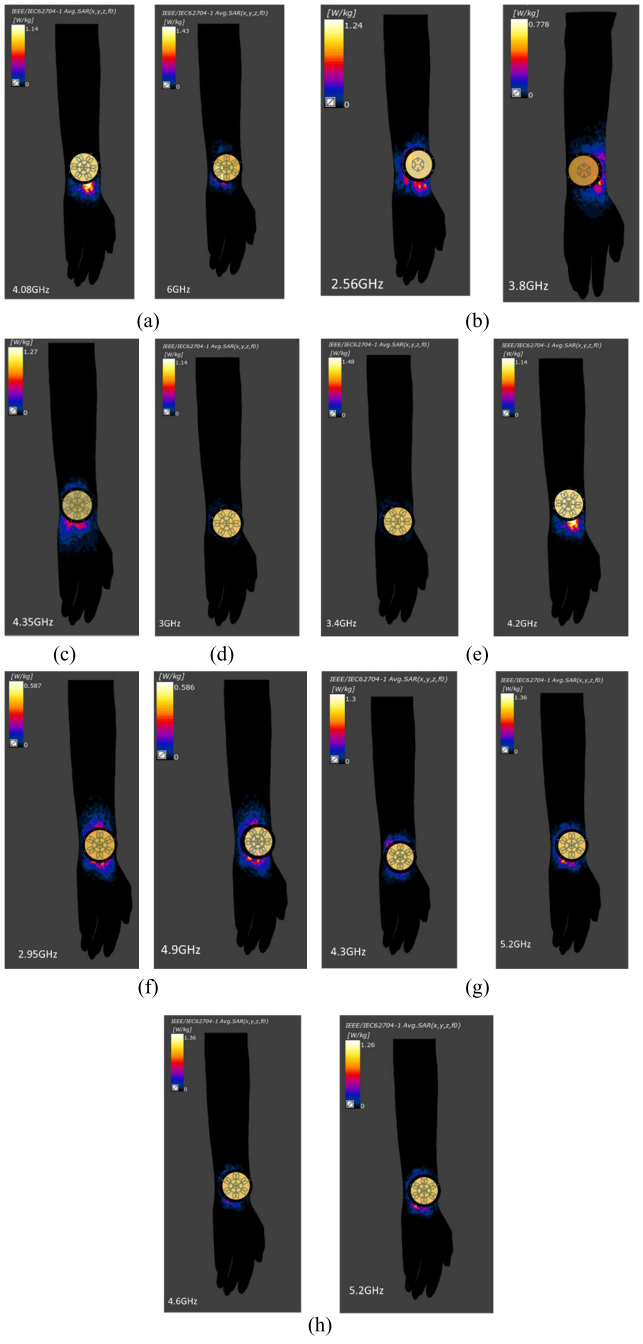

FIGURE 15. Analyzed SAR values for the 8 modes. State (a) A, (b) B, (c) C, (d) D, (e) E, (f) F, (g) G, and (h) H.

the real number, $\vec{E}$ is denoted as the electric field, and $\vec{H}^*$ is denoted as the conjugate magnetic field:

$$\vec{S}(x, y, z) = \left(\frac{1}{2}\right)\left(\vec{E}(x, y, z) \times \vec{H}^*(x, y, z)\right). \tag{2}$$

The average power density of the electromagnetic field human exposure standard is presented by (3):

$$S_{av}(z = d) = \max\left(\left(\frac{1}{A}\right)\int_A \vec{S}(x, y, z) \cdot \hat{z}dxdy\right) \tag{3}$$

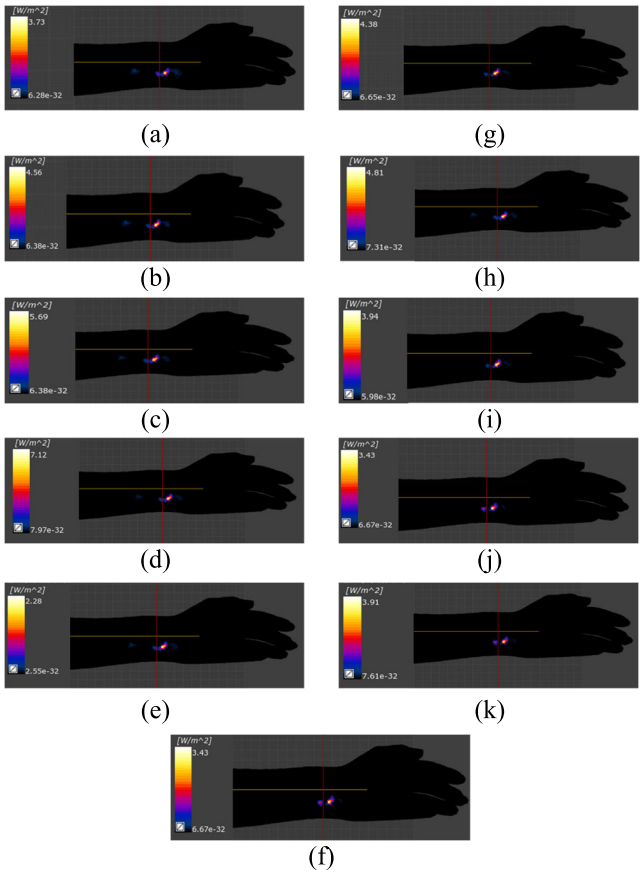

FIGURE 16. PD simulation of the 11 modes explored by the V-band. (a) State 1. (b) State 2. (c) State 3. (d) State 4. (e) State 5. (f) State 6. g) State 7. (h) State 8. (i) State 9. (j) State 10. (k) State 11.

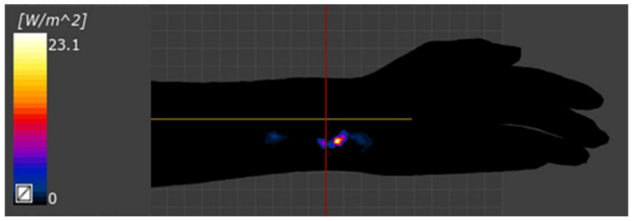

FIGURE 17. PD simulation of D-band at 144GHz.

where A is the average power density area and d is the distance between areas. Equation (3) illustrates the sum of power through the area A at a specific distance (z = d). IEEE and FCC proposed the use of power density for analysis above 6 GHz, and its specification in every 1 cm^2 and 4 cm^2 square area need to be less than 40 (W/m^2) power density value. Fig. 16 shows the power density analysis of the 11 simulated modes at 47 GHz, and the value area is set to 4 cm^2. The power density values of the 11 modes are much lower than the standard 40(W/m2). The reason for this result is that there is a sub-6GHz antenna ground between the designed V-band antenna and human tissue, so that the antenna radiation is blocked by the ground. Fig. 17 shows the simulation of the

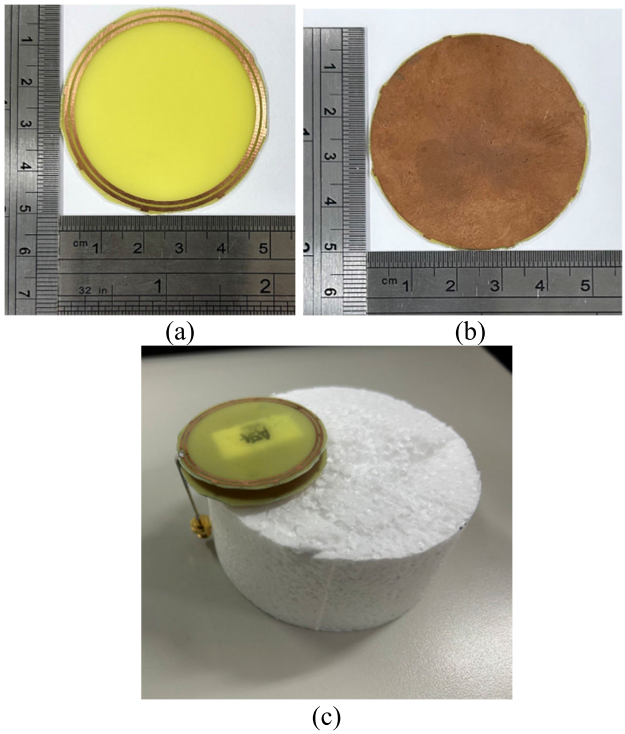

FIGURE 18. Prototype of the dual loop antenna. (a) Top view. (b) Bottom view. (c) Side view.

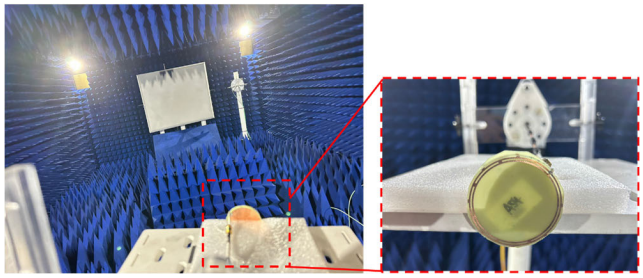

FIGURE 19. Darkroom environment and antenna setup for actual measurements.

PD value of the D-band antenna at 144GHz, which is also in line with the standard for commercial sales.

IV. MEASUREMENT RESULTS

A. DUAL LOOP ANTENNA DESIGN FOR SUB-6 GHz

Fig. 18 shows the actual structure dimensions of the dual loop antenna. Fig. 19 is the darkroom environment and antenna setup for the actual measurements. Eight modes of measurement and simulated reflection coefficients are listed in Fig. 20. In Fig. 20(a), the reflection coefficient of mode A below −6 dB produces resonances at 2.3, 4.1 and 5.8 GHz, and the simulation and measurement results are consistent. Measurements in mode B resulted in resonance at 2.5 and 3.9 GHz, but deeper resonance points were obtained at the higher frequency of 6.8 GHz. The mode C in Fig. 20(b) shows that the low frequency produces two resonances at 2.2 and 3 GHz, but the resonance point disappears at the high

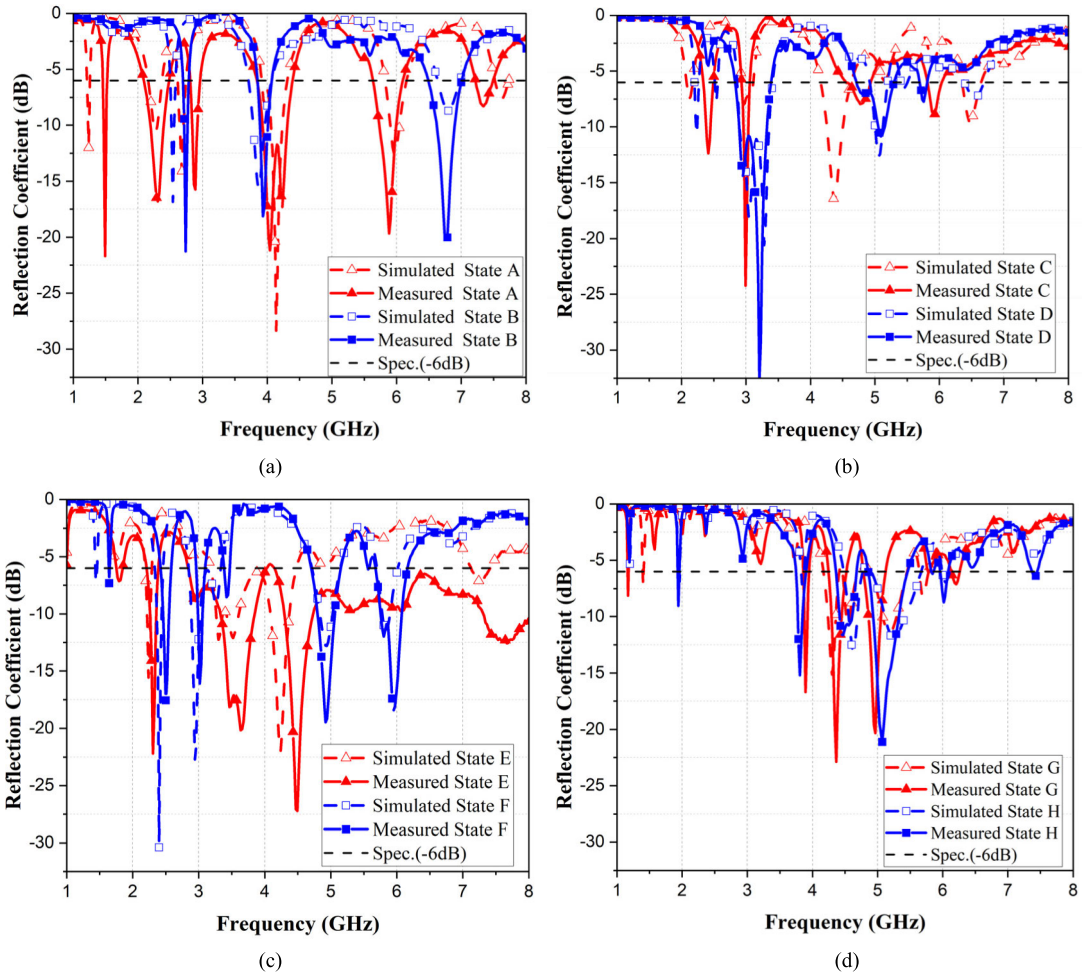

FIGURE 20. Comparison of simulated and measured coefficients in each mode.

TABLE 3. Reflection coefficients of dual loop antennas in 11modes.

State	Sim. (GHz)	Meas. (GHz)	State	Sim. (GHz)	Meas. (GHz)
A	2.24-2.3 2.66-2.7 4.08-4.23 5.9-6.04	2.2-2.4 2.8-2.9 3.9-4.3 5.73-6	E	3.27-3.6 4-4.38	2.26-2.35 3.33-3.85 4.3-4.72 7.3-8
B	2.51-2.57 3.78-3.97	2.72- 2.75 3.89- 4.01 6.6-6.9	F	2.38-2.42 2.9-3.02 4.84-5.02 5.78-5.88	2.44-2.55 2.98-3.05 4.8-5.05 5.75-6.05
C	4.25-4.51	2.3- 2.45 2.9-3.1	G	4.24-4.36 4.52-4.58 5.06-5.3	3.89-3.91 4.34.45 4.87-5
D	2.9-3.35	2.9- 3.33	H	4.56-4.68 5.1-5.42	3.7-3.82 4.4-4.62 4.94-5.3

frequency of 4.3 GHz. The measured and simulated results in mode D are consistent, and the two resonances are generated at 2.9 and 3.2 GHz. The mode E in Fig. 20(c) shows better impedance matching results in the measurement, and better resonance effects are obtained at the same 3.8 and 4.5 GHz bands. Mode F shows good simulation and measurement results with good agreement at 2.45, 3, 4.9 and 6 GHz. The measured and simulated results of the mode G in Fig. 20(d) show that the frequency band is shifted to the lower frequency. Mode H demonstrates both simulated and measured agreement, resonating at 4.5 and 5 GHz. The measured and simulated reflection coefficients are summarized in Table 3. Fig. 21 shows the comparison of the measured and simulated gains for the eight modes. Fig. 21(a) and (b) shows that the average gain of the design is 2.5 dBi.

The xy, yz and xz-plane radiation patterns for Modes A-H are shown in Fig. 22. From the results, the simulation and measurement of the radiation patterns are consistent when the antenna is operating in free space.

B. V-BAND VIVALDI ANTENNA MEASUREMENT RESULTS

Fig. 23(a) is the actual antenna structure size, and Fig. 23(b) is the actual darkroom measurement environment and antenna

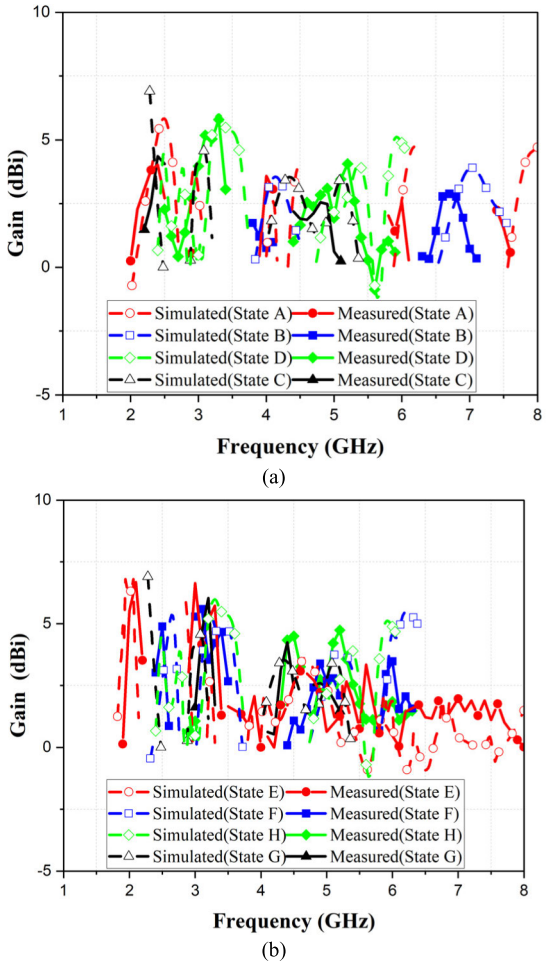

FIGURE 21. Comparison of measured and simulated gain.

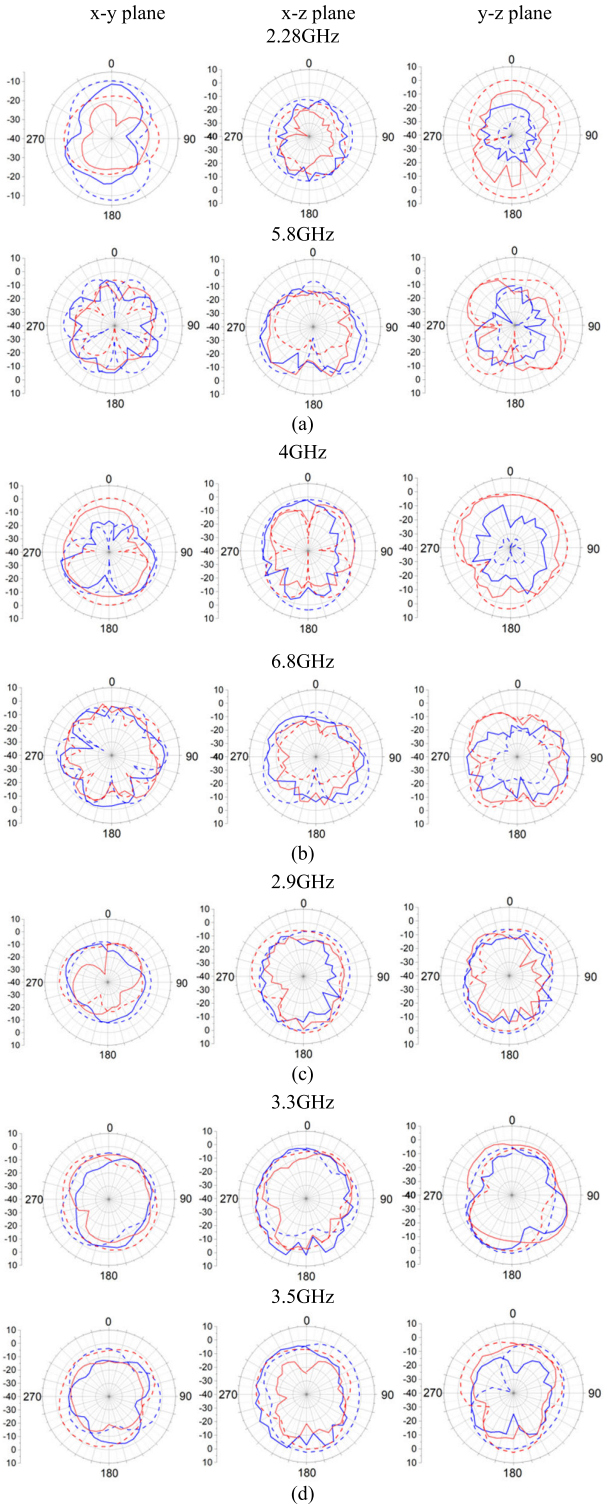

FIGURE 22. Sub-6 GHz antenna radiation pattern of state (a) A, (b) B, (c) C, (d) D.

setup. A comparison of the measured and simulated reflection coefficients for 11 modes is in Fig. 24. Fig. 24(a) shows that the measured bandwidth of modes 1-3 at the −10 dB reflection coefficient standard covers 45.1-48.7 GHz, which is similar to the simulated 45-48 GHz. Modes 4-6 of Fig. 24(b) show the bandwidth covering the operating band of 41-50 GHz. The bandwidth of Modes 7-9 in Fig. 24(c) is shown at about 41-49 GHz. Fig. 24(d) shows that the reflectance coefficients of modes 10 and 11 cover 41-49 GHz, but the reflectance coefficient in mode 11 is poor. The measured reflection coefficients of the 11 modes are concentrated in the range of 40-50GHz, which means that the operating frequency band will not be affected when switching short circuits. Table 4 presents the comparison of the measured and simulated reflection coefficients for all modes of diode switching and measurement.

Fig. 25 shows the comparison of the measured and simulated gains for all modes. The highest radiation gain of about 10 dBi can be achieved for mode 1 in Fig. 25(a), and the average radiation gain decreases to about 7-8 dBi when increasing the number of shorts to modes 2 and 3. Fig. 25(b) has an average measurement gain of about 6-7 dBi for mode 4-6, which decreases to 5-7 dBi at 45-50 GHz.The measured gain of Modes 7-9 in Fig. 25(c) shows that the radiation gain trends of the three modes are similar, with an average gain of 6.5-8 dBi. In Fig. 25(d), the average gain of modes

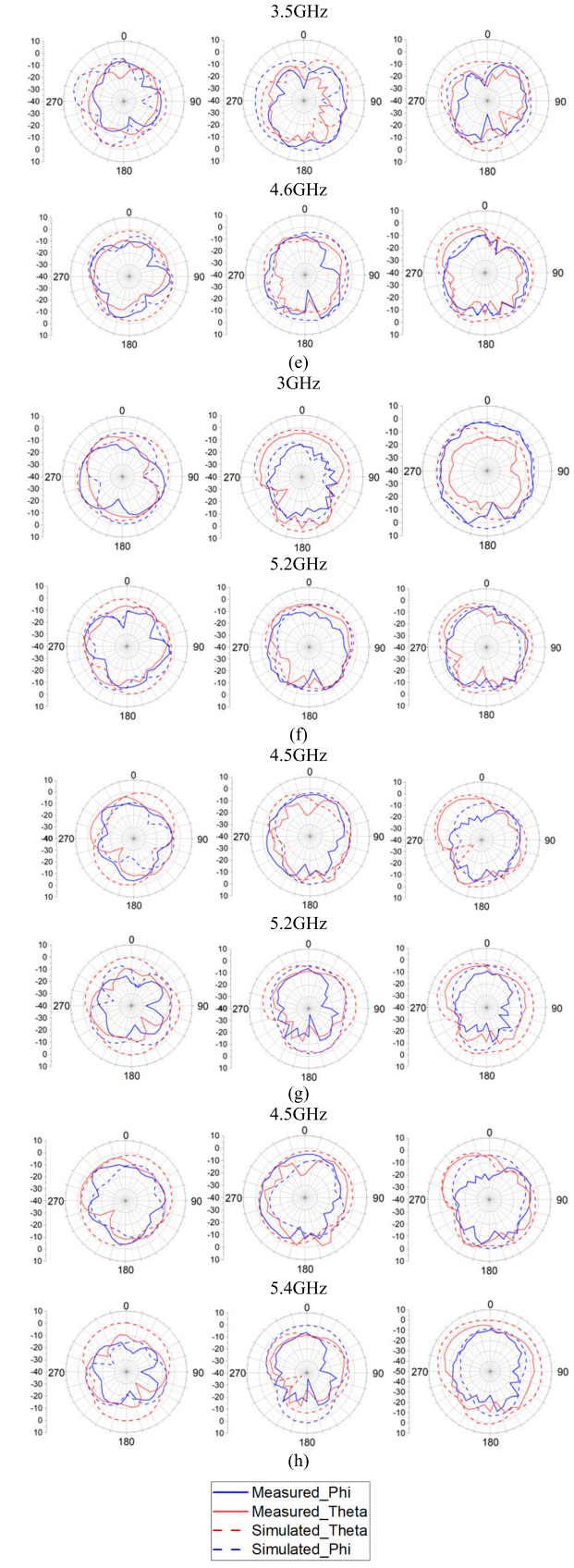

FIGURE 22. *(Continued.)* **Sub-6 GHz antenna radiation pattern of state (e) E, (f) F, (g) G, and (h) H.**

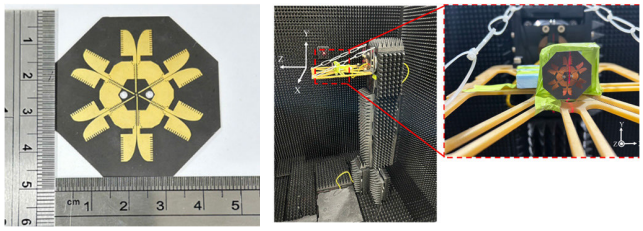

FIGURE 23. **(a) Antenna prototype. (b) Darkroom measurement environment.**

TABLE 4. **Comparison of diode switching and full mode bandwidth.**

State	Diode Switch	Sim.(GHz)	Meas.(GHz)
1	000001	45-48	45.1-48.7
2	000011	48.39-50	46.45-49.85
3	000101	42.8-46.3	43.6-50
4	001001	42.59-46.19	43.2-45.6 47.35-50
5	000111	41.9-50.22	41.8-50
6	001011	41.34-48.3	41.75-48.9
7	010101	41.32-48.13	42.35-47.4
8	001111	41.7-48.7	42.8-48.65
9	010111	41.55-48.49	43.05-49.65
10	011111	41.76-48.26	41.95-47.6
11	111111	41.97-47.89	43.05-49.65

10 and 11 is 6-7 dBi. The results show that the radiation gain decreases when the number of shorts is gradually increased.

The xy-plane radiation patterns of 11 modes at 48 GHz are shown in Fig. 26. The mode 1 of Fig. 26(a) has the same radiation directivity in both measured and simulated radiation fields. However, the maximum value of the measurement result is at the 105 degrees, which may be caused by the measurement setup error. The radiation pattern of mode 2 in Fig. 26(b) shows that the pattern is shifted at 90 degrees and 150 degrees due to the additional short-circuit contacts. For mode 3 in Fig. 26(c), the beams are concentrated at 90 and 210 degrees. The main beam of mode 4 in Fig. 26(d) is concentrated at 90 and 270 degrees, respectively. The mode 5 in Fig. 26 (e) is distributed between 90 and 210 degrees. In Fig. 26(f), the main beam of mode 6 is concentrated at 90-150 degrees and 270 degrees respectively, but the measurement results show that the radiation gain at 270 degrees is smaller. The mode 7 of Fig. 26(g) is distributed at 90°, 210° and 330° respectively. Mode 9 in Fig. 26(i) shows that the beams have been radiating omnidirectionally at nearly 360 degrees, while mode 10 in Fig. 26(j) also shows the same radiation trend. The mode 11 in Fig. 26(k) shows the omnidirectional radiation pattern.

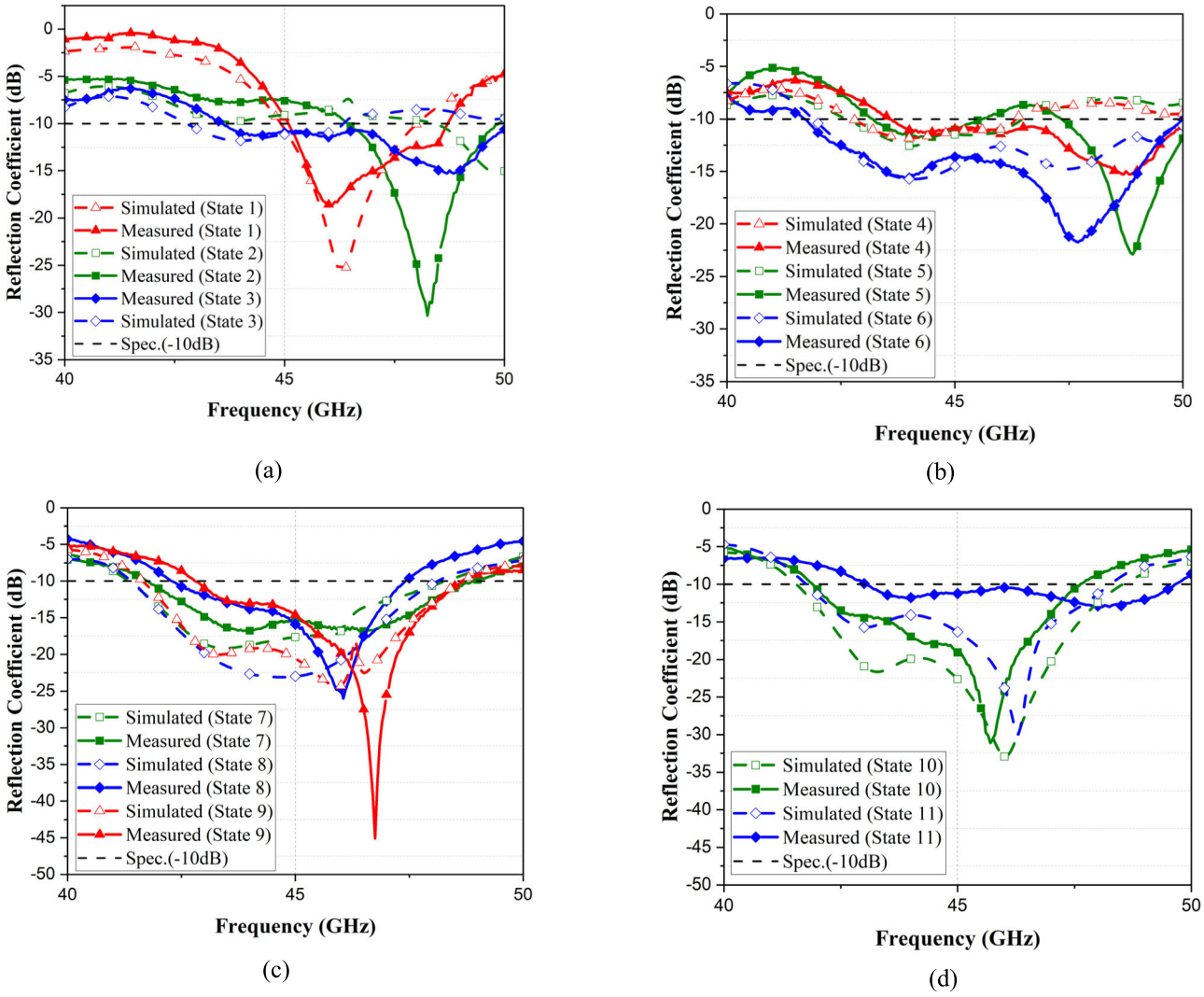

FIGURE 24. Reflection coefficient of V-band. (a) State 1-3. (b) State 4-6. (C) State 7-9. (d) State 10-11.

C. D-BAND ANTENNA MEASUREMENT RESULTS

Fig. 27(a) and (b) show the size of the front and back of the designed D-band diamond-shaped monopole antenna, which is 18.75 × 18.75 mm^2 mm. The measurement environment is shown in Figure 24(c). The antenna is screwed to the WR-6.5 waveguide by a VDI expander to convert the frequency band to 110-170 GHz and analyzed with the MS4644B network analyzer.

Fig. 28 analyzes the simulated and measured reflectance coefficients. The simulated reflectance coefficients have a bandwidth of 138.9-147 GHz at −10 dB standard, while the measured reflection coefficients cover 139.6-164.3 GHz.

The results show that both the measurement and simulation resonate at about 144 GHz, but the measurement result has a wider operating bandwidth. The reason for the large difference between the measured and simulated results may be due to the thin thickness of the plate, which allows the screws to bend the antenna when fixing the structure, resulting in a change in the matching structure. Comparing the measured and simulated gains in Fig. 29, the highest measured gain is about 12 dBi on average, and the trend is greater than the simulated results. Fig. 30 shows a comparison of the measured and simulated radiation fields of the antenna at 144 GHz, and due to the limitation of the measurement environment, it is not possible to measure the fields from 90 degrees to 270 degrees. Fig. 30(a) depicts the measurement results in the yz-plane. The measured radiation pattern is consistent with the simulated results, with the maximum radiation gain at 0 degrees.

D. D-BAND ANTENNA MEASUREMENT RESULTS

Table 5 shows that the design of reconfigurable antennas in recent years has focused more on the Sub-6 GHz and millimeter wave bands and no higher frequency band is discussed. The antenna designed in this paper is a combination of sub-6GHz, V-band and D-band and can be used in most

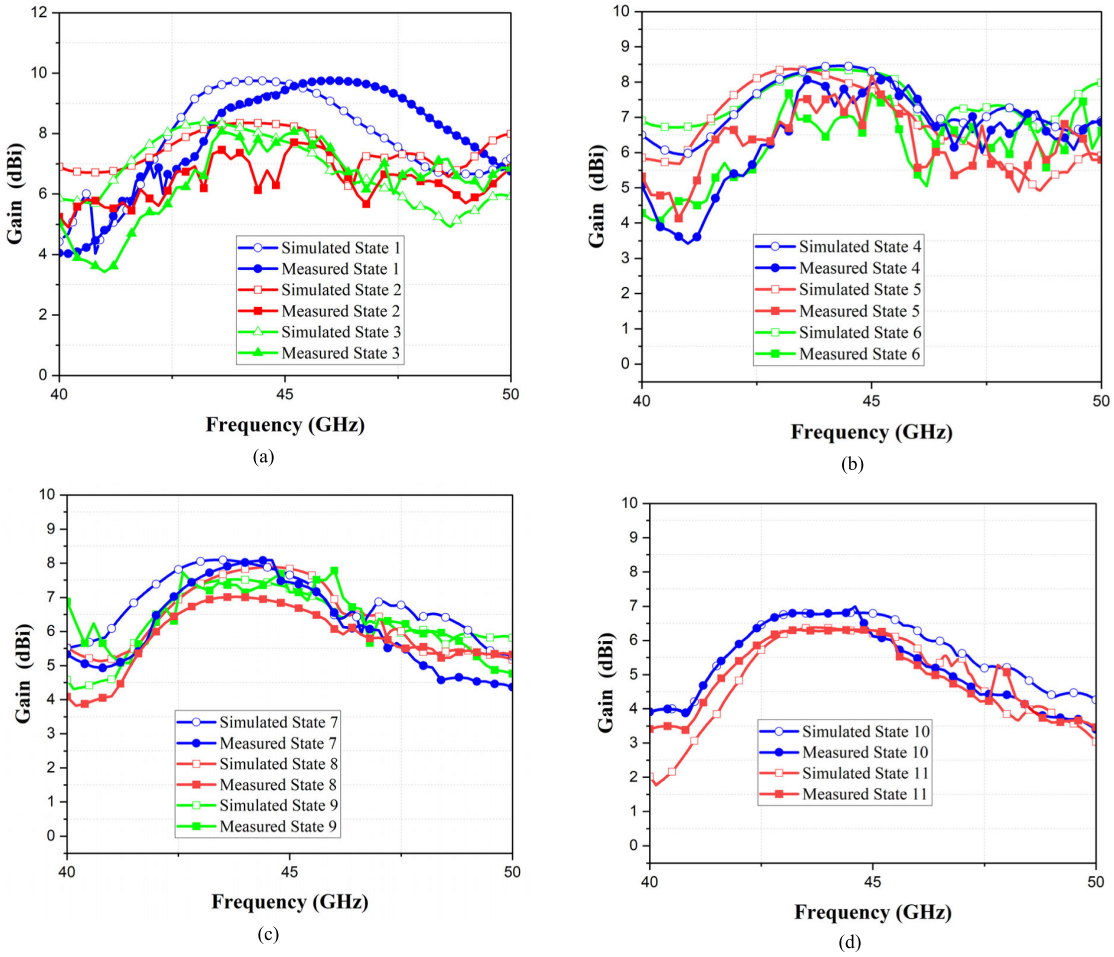

FIGURE 25. Measured and simulated gains for all modes. (a) State 1-3. (b) State 4-6. (C) State 7-9. (d) State 10-11.

TABLE 5. Comparison of reconfigurable antennas in recent years.

Ref.	PORT	Frequency (GHz)	Peak Gain(dBi)	BW%	Size (mm^2)
Pro.	3	2.4/4.5/5.75/6.9 45 140	0-5 5-10 12	18.2/3.3/5.08/4.44 19.78 16.25	50×50
[10]	2	2.23-3.69 19.32-32.90	1.06-2.92 13.09	49.3 52	52.5×16
[26]	2	9.8-10.2 26.5-29	14.8 24.4	6 10.7	85×85
[28]	2	2.4-2.47 27.7-28.3	8.1-15	2.8、1.4	75×75
[29]	12	2.5/3.5/5.5/7.5/28	1-5.5 6.5	-	55×55(Single Antenna)
[30]	2	2.4、5.2、60	3.97 4.07 12.29	-	-
[31]	2	3.5、60	7.3 24	2.3 5.3	80 ×86
[33]	2	2.4-2.485 5.15-5.85 57-64	9.8 7.9 8.4	80	140 ×140
[34]	2	3.12–3.84 24.9–30.6	6.3-7.1 9.2-11.3	20.7 5.6	43×33.9
[48]	2	3.2-4.05 26.8-29.55	7.27-10.44 11.8-14.6	23.45 9.76	92 × 92

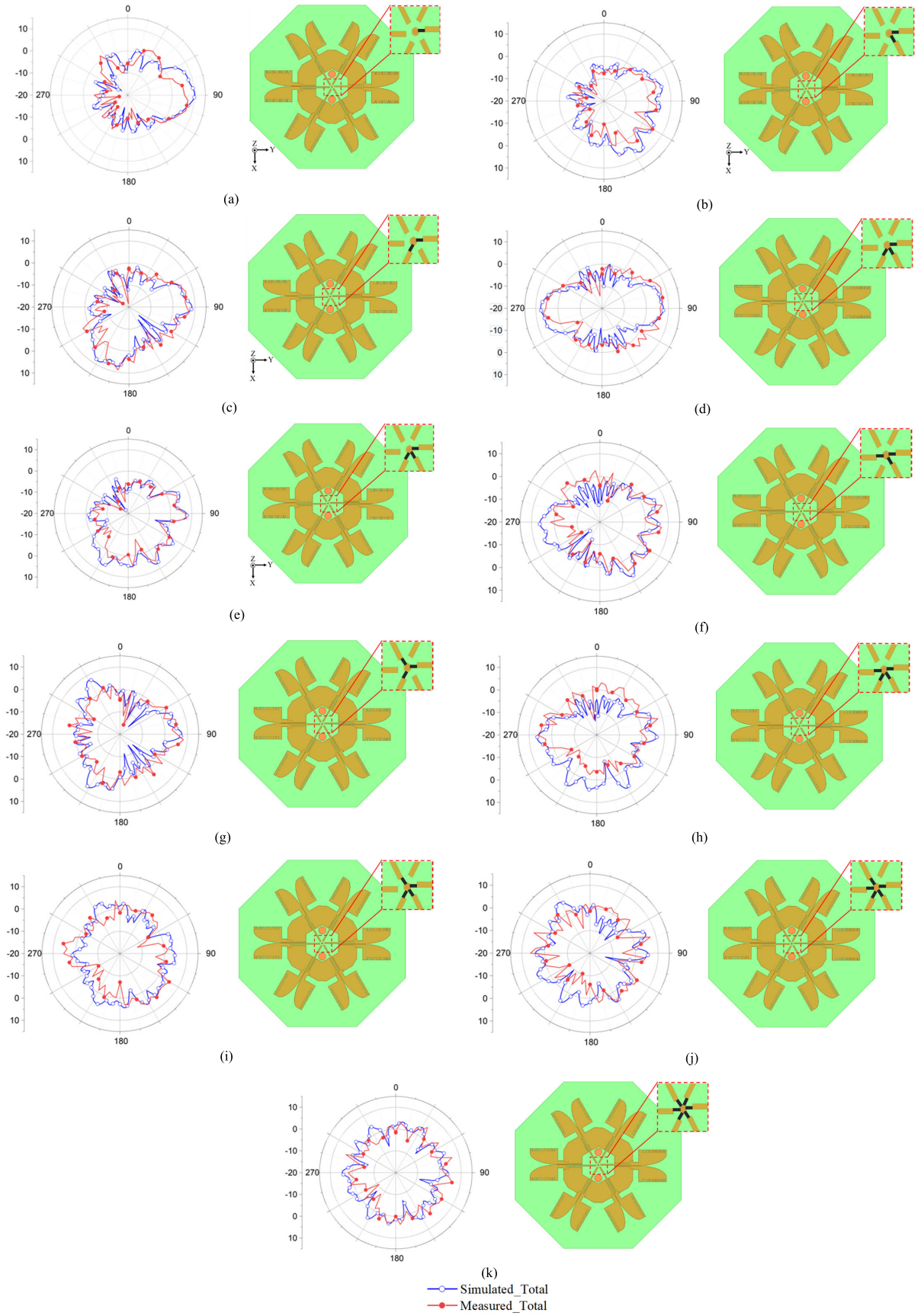

FIGURE 26. The xy-plane radiation field pattern for all modes. (a) State 1. (b) State 2. (c) State 3. (d) State 4. (e) State 5. (f) State 6. (g) State 7. (h) State 8. (i) State 9. (j) State 10. (k) State 11.

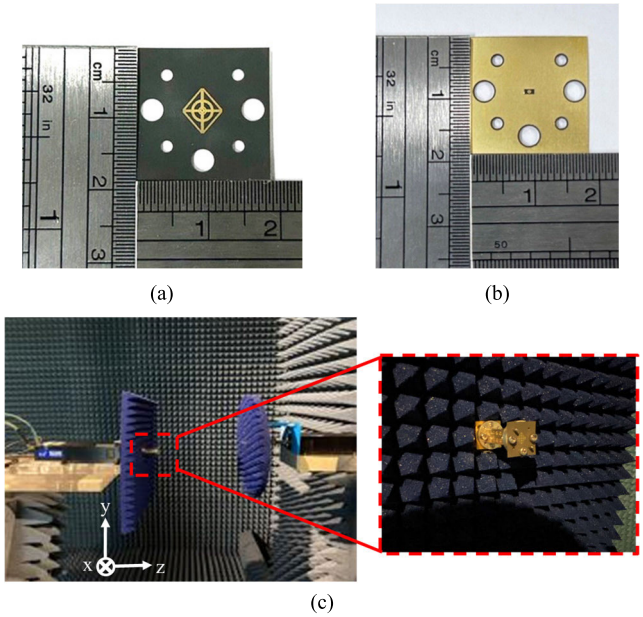

FIGURE 27. Prototype of the diamond-shaped antenna. (a) Front side. (b) Reverse side. (c) Measurement environment.

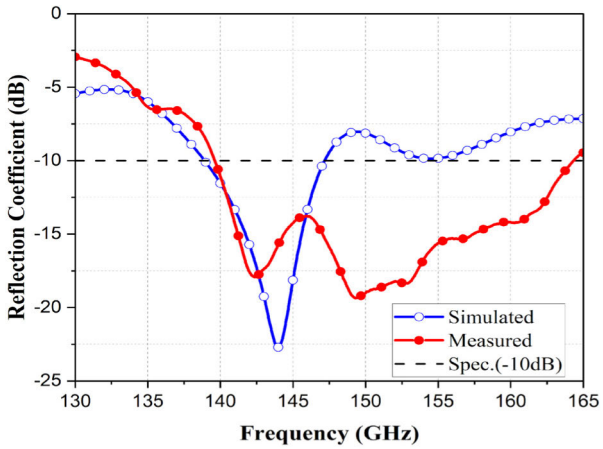

FIGURE 28. D-band diamond-shaped monopole reflection coefficient.

communication applications. The design of dual loop antennas in the sub-6 GHz band can be designed by switching 8 different modes through a diode switch to meet the design requirements, such as 2-2.4, 4.3-4.7, 5.75-6.05, and 6.6-6.9 GHz bands. Also, the gain at low frequencies is higher compared to the literature [10], [29], [30]. In this paper, the V-band achieves beam switching from 0 to 360 degrees by diode switching and achieves a fractional bandwidth of 19.78% (41-50 GHz), which has a wider bandwidth compared with the literature [26], [27], [28], [31], [33]. Compared with literature [34], [48], there are more optional frequency bands and beam directions. The measured maximum gain can reach a maximum gain of 12dBi, indicating that this structure can also be used for high power signal transmission at very close distances.

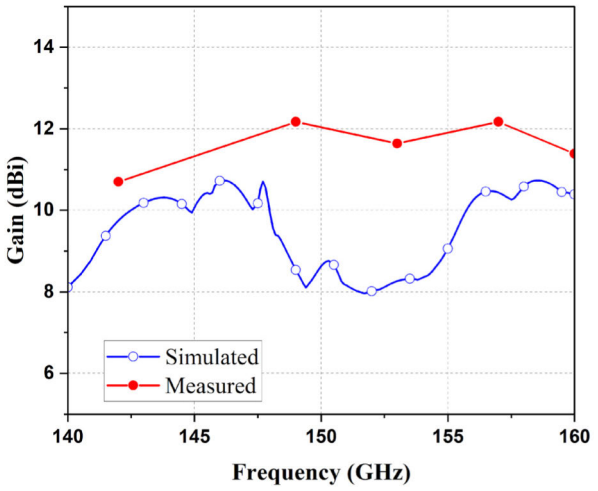

FIGURE 29. Comparison of measured and simulated gain.

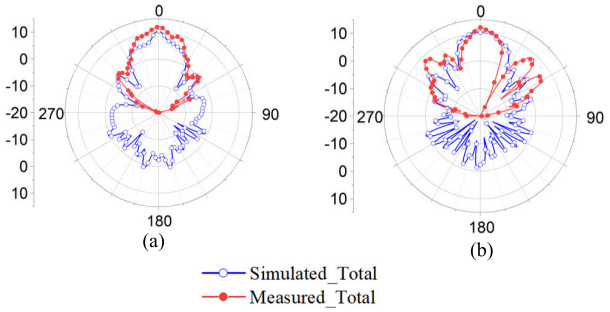

FIGURE 30. Planar radiation pattern at 144 GHz in (a) yz plane (b) xz plane.

V. CONCLUSION

This paper proposes a multi-layer structure of multi-band wearable reconfigured antenna, which can switch 8 different modes at sub-6 GHz through multiple diode switches to reach multiple frequency bands such as 2-2.4, 4.3-4.7, 5.75-6.05, and 6.6-6.9 GHz. In the millimeter wave band, the Vivaldi antenna in the V-band is also used to achieve a controllable beam from 0 to 360 degrees through diode switching. And the reflection coefficient can cover 19.78% (41-50GHz) of the fractional bandwidth. The D-band diamond-shaped monopole antenna has a reflection coefficient that covers 16.25% (139.6-164.3 GHz) of the fractional bandwidth and has directional radiation that can reach a maximum of 12 dBi. Considering the effect of antenna radiation on human body, the results show that the SAR value and PD generated at sub-6GHz and V-band are lower than the international definition of SAR value of 1g human tissue at 1.6 W/kg, and the power density at 4cm^2 area is lower than 40(W/m^2), which means the designed antenna can be used in wearable devices. The antenna architecture can well meet the needs of multi-band and multi-beam direction, making it a good prospect for development.

REFERENCES

[1] M. Zada, I. A. Shah, and H. Yoo, "Integration of sub-6-GHz and mm-wave bands with a large frequency ratio for future 5G MIMO applications," *IEEE Access*, vol. 9, pp. 11241–11251, 2021.

[2] H. Wang, K. E. Kedze, and I. Park, "A high-gain and wideband series-fed angled printed dipole array antenna," *IEEE Trans. Antennas Propag.*, vol. 68, no. 7, pp. 5708–5713, Jul. 2020.

[3] K. Sultan, M. Ikram, and N. Nguyen-Trong, "A multiband multibeam antenna for sub-6 GHz and mm-wave 5G applications," *IEEE Antennas Wireless Propag. Lett.*, vol. 21, pp. 1278–1282, 2022.

[4] J. H. Bae and Y. J. Yoon, "5G dual (S-/Ka-) band antenna using thick patch containing slotted cavity array," *IEEE Antennas Wireless Propag. Lett.*, vol. 20, pp. 1008–1012, 2021.

[5] Y. Zhang, J.-Y. Deng, D. Sun, J.-Y. Yin, and L.-X. Guo, "Compact slow-wave SIW H-plane horn antenna with increased gain for vehicular millimeter wave communication," *IEEE Trans. Veh. Technol.*, vol. 70, no. 7, pp. 7289–7293, Jul. 2021.

[6] M. Ikram, N. Nguyen-Trong, and A. M. Abbosh, "Common-aperture sub-6 GHz and millimeter-wave 5G antenna system," *IEEE Access*, vol. 8, pp. 199415–199423, 2020.

[7] C. Gu, S. Gao, V. Fusco, G. Gibbons, B. Sanz-Izquierdo, A. Standaert, P. Reynaert, W. Bösch, M. Gadringer, R. Xu, and X. Yang, "A D-band 3D-printed antenna," *IEEE Trans. THz Sci. Technol.*, vol. 10, no. 5, pp. 433–442, Sep. 2020.

[8] S. Erdogan, K. J. Moon, M. Kathaperumal, and M. Swaminathan, "D-band integrated and miniaturized quasi-Yagi antenna array in glass interposer," *IEEE Trans. THz Sci. Technol.*, vol. 13, no. 3, pp. 270–279, May 2023.

[9] A. J. Alazemi, H.-H. Yang, and G. M. Rebeiz, "Double bow-tie slot antennas for wideband millimeter-wave and terahertz applications," *IEEE Trans. THz Sci. Technol.*, vol. 6, no. 5, pp. 682–689, Sep. 2016.

[10] J.-X. Chen, S.-H. Cao, and X.-F. Zhang, "SPPs-shared dual-band antenna with large frequency ratio," *IEEE Access*, vol. 8, pp. 29132–29139, 2020.

[11] S. Islam, M. Zada, and H. Yoo, "Highly compact integrated sub-6 GHz and millimeter-wave band antenna array for 5G smartphone communications," *IEEE Trans. Antennas Propag.*, vol. 70, no. 12, pp. 11629–11638, Dec. 2022.

[12] C.-K. Hsu and S.-J. Chung, "Compact antenna with U-shaped open-end slot structure for multi-band handset applications," *IEEE Trans. Antennas Propag.*, vol. 62, no. 2, pp. 929–932, Feb. 2014.

[13] S. X. Ta, H. Choo, I. Park, and R. W. Ziolkowski, "Multi-band, wide-beam, circularly polarized, crossed, asymmetrically barbed dipole antennas for GPS applications," *IEEE Trans. Antennas Propag.*, vol. 61, no. 11, pp. 5771–5775, Nov. 2013.

[14] F. Jia, Z. Zheng, Q. Wang, P. Liu, S. Liao, W. Che, and Q. Xue, "A new multi-band multi-array antenna configuration with scattering suppression for radiation pattern distortion mitigation of base station," *IEEE Trans. Antennas Propag.*, vol. 70, no. 7, pp. 6006–6011, Jul. 2022.

[15] A. Foudazi, H. R. Hassani, and S. Mohammad ali nezhad, "Small UWB planar monopole antenna with added GPS/GSM/WLAN bands," *IEEE Trans. Antennas Propag.*, vol. 60, no. 6, pp. 2987–2992, Jun. 2012.

[16] X. Lu, Y. Chen, S. Guo, and S. Yang, "An electromagnetic-transparent cascade comb dipole antenna for multi-band shared-aperture base station antenna array," *IEEE Trans. Antennas Propag.*, vol. 70, no. 4, pp. 2750–2759, Apr. 2022.

[17] Y. Chen, B. Ai, Y. Niu, R. He, Z. Zhong, and Z. Han, "Resource allocation for device-to-device communications in multi-cell multi-band heterogeneous cellular networks," *IEEE Trans. Veh. Technol.*, vol. 68, no. 5, pp. 4760–4773, May 2019.

[18] K. Trzebiatowski, M. Rzymowski, L. Kulas, and K. Nyka, "Simple 60 GHz switched beam antenna for 5G millimeter-wave applications," *IEEE Antennas Wireless Propag. Lett.*, vol. 20, pp. 38–42, 2021.

[19] S. Cheng, P. Rantakari, R. Malmqvist, C. Samuelsson, T. Vaha-Heikkila, A. Rydberg, and J. Varis, "Switched beam antenna based on RF MEMS SPDT switch on quartz substrate," *IEEE Antennas Wireless Propag. Lett.*, vol. 8, pp. 383–386, 2009.

[20] L. Wu, A. J. Farrall, and P. R. Young, "Substrate integrated waveguide switched beam antenna," *IEEE Trans. Antennas Propag.*, vol. 63, no. 5, pp. 2301–2305, May 2015.

[21] A. E. I. Lamminen, S. K. Karki, A. Karttunen, M. Kaunisto, J. Säily, M. Lahdes, J. Ala-Laurinaho, and V. Viikari, "Beam-switching dual-spherical lens antenna with low scan loss at 71–76 GHz," *IEEE Antennas Wireless Propag. Lett.*, vol. 17, pp. 1871–1875, 2018.

[22] M. Rzymowski and L. Kulas, "Two-row ESPAR antenna with simple elevation and azimuth beam switching," *IEEE Antennas Wireless Propag. Lett.*, vol. 20, pp. 1745–1749, 2021.

[23] H. Xu, B.-Z. Zhang, J.-p. Duan, J. Cui, Y. Xu, Y. Tian, L. Yan, M. Xiong, and Q. Jia, "Wide solid angle beam-switching conical conformal array antenna with high gain for 5G applications," *IEEE Antennas Wireless Propag. Lett.*, vol. 17, pp. 2304–2308, 2018.

[24] K.-S. Kim, J.-S. Yoo, J.-W. Kim, S. Kim, J.-W. Yu, and H. L. Lee, "All-around beam switched antenna with dual polarization for drone communications," *IEEE Trans. Antennas Propag.*, vol. 68, no. 6, pp. 4930–4934, Jun. 2020.

[25] Y. Yashchyshyn, K. Derzakowski, G. Bogdan, K. Godziszewski, D. Nyzovets, C. H. Kim, and B. Park, "28 GHz switched-beam antenna based on S-PIN diodes for 5G mobile communications," *IEEE Antennas Wireless Propag. Lett.*, vol. 17, pp. 225–228, 2018.

[26] P. Mei, S. Zhang, and G. F. Pedersen, "A dual-polarized and high-gain *X-/Ka*-band shared-aperture antenna with high aperture reuse efficiency," *IEEE Trans. Antennas Propag.*, vol. 69, no. 3, pp. 1334–1344, Mar. 2021.

[27] T. Li and Z. N. Chen, "Shared-surface dual-band antenna for 5G applications," *IEEE Trans. Antennas Propag.*, vol. 68, no. 2, pp. 1128–1133, Feb. 2020.

[28] J. Zhu, Y. Yang, S. Liao, S. Li, and Q. Xue, "Dual-band aperture-shared Fabry–Pérot cavity-integrated patch antenna for millimeter-wave/sub-6 GHz communication applications," *IEEE Antennas Wireless Propag. Lett.*, vol. 21, pp. 868–872, 2022.

[29] N. Hussain and N. Kim, "Integrated microwave and mm-wave MIMO antenna module with 360° pattern diversity for 5G Internet of Things," *IEEE Internet Things J.*, vol. 9, no. 24, pp. 24777–24789, Dec. 2022.

[30] Y. R. Ding and Y. J. Cheng, "A tri-band shared-aperture antenna for (2.4, 5.2) GHz Wi-Fi application with MIMO function and 60 GHz Wi-Gig application with beam-scanning function," *IEEE Trans. Antennas Propag.*, vol. 68, no. 3, pp. 1973–1981, Mar. 2020.

[31] J. F. Zhang, Y. J. Cheng, Y. R. Ding, and C. X. Bai, "A dual-band shared-aperture antenna with large frequency ratio, high aperture reuse efficiency, and high channel isolation," *IEEE Trans. Antennas Propag.*, vol. 67, no. 2, pp. 853–860, Feb. 2019.

[32] J. Zhu, Y. Yang, Z. Hou, S. Liao, and Q. Xue, "Dual-band aperture-shared high gain antenna for millimeter-wave multi-beam and sub-6 GHz communication applications," *IEEE Trans. Antennas Propag.*, vol. 70, no. 6, pp. 4848–4853, Jun. 2022.

[33] X. Yang, L. Ge, Y. Ji, X. Zeng, Y. Li, C. Ding, J. Sun, and K.-M. Luk, "An integrated tri-band antenna system with large frequency ratio for WLAN and WiGig applications," *IEEE Trans. Ind. Electron.*, vol. 68, no. 5, pp. 4529–4540, May 2021.

[34] J. Lan, Z. Yu, J. Zhou, and W. Hong, "An aperture-sharing array for (3.5, 28) GHz terminals with steerable beam in millimeter-wave band," *IEEE Trans. Antennas Propag.*, vol. 68, no. 5, pp. 4114–4119, May 2020.

[35] P. Lu, T. Haddad, B. Sievert, B. Khani, S. Makhlouf, S. Dülme, J. F. Estévez, A. Rennings, D. Erni, U. Pfeiffer, and A. Stöhr, "InP-based THz beam steering leaky-wave antenna," *IEEE Trans. THz Sci. Technol.*, vol. 11, no. 2, pp. 218–230, Mar. 2021.

[36] Z. Fang, H. Yang, Y. Gao, F. Zhai, J. W. Wu, Q. Cheng, and T. J. Cui, "Design of a 2-bit reconfigurable UWB planar antenna array for beam scanning application," *IEEE Open J. Antennas Propag.*, vol. 4, pp. 91–96, 2023.

[37] F. A. Asadallah, H. A. Khalek, B. A. A. Modad, J. A. Hosn, J. Costantine, R. Kanj, and Y. Tawk, "Spectrum-aware compact reconfigurable UHF antenna for interweave cognitive radio," *IEEE Open J. Antennas Propag.*, vol. 4, pp. 69–73, 2023.

[38] U. Musa, S. M. Shah, H. A. Majid, Z. Z. Abidin, M. S. Yahya, S. Babani, and Z. Yunusa, "Recent advancement of wearable reconfigurable antenna technologies: A review," *IEEE Access*, vol. 10, pp. 121831–121863, 2022.

[39] C. Liu, Y. Li, T. Liu, Y. Han, J. Wang, and S. Qu, "Polarization reconfigurable and beam-switchable array antenna using switchable feed network," *IEEE Access*, vol. 10, pp. 29032–29039, 2022.

[40] S. Haydhah, R. Gold, Z. Dong, F. Ferrero, L. Lizzi, M. S. Sharawi, and A. A. Kishk, "Multifunction pattern reconfigurable slot-antenna for 5G sub-6 GHz small-cell base-station applications," *IEEE Access*, vol. 11, pp. 69056–69071, 2023.

[41] M. S. Yahya, S. Soeung, S. K. A. Rahim, U. Musa, S. S. B. Hashwan, and M. A. Haque, "Machine learning-optimized compact frequency reconfigurable antenna with RSSI enhancement for long-range applications," *IEEE Access*, vol. 12, pp. 10970–10987, 2024.

[42] S. Padmanathan, A. A. Al-Hadi, A. M. Elshirkasi, S. S. Al-Bawri, M. T. Islam, T. Sabapathy, M. Jusoh, P. Akkaraekthalin, and P. J. Soh, "Compact multiband reconfigurable MIMO antenna for sub-6 GHz 5G mobile terminal," *IEEE Access*, vol. 10, pp. 60241–60252, 2022.
[43] K. R. Jha, N. Rana, and S. K. Sharma, "Design of compact antenna array for MIMO implementation using characteristic mode analysis for 5G NR and Wi-Fi 6 applications," *IEEE Open J. Antennas Propag.*, vol. 4, pp. 262–277, 2023.
[44] Z. Chen, Y. Liu, T. Yuan, and H. Wong, "A miniaturized MIMO antenna with dual-band for 5G smartphone application," *IEEE Open J. Antennas Propag.*, vol. 4, pp. 111–117, 2023.
[45] O. Sokunbi, H. Attia, A. Hamza, A. Shamim, Y. Yu, and A. A. Kishk, "New self-isolated wideband MIMO antenna system for 5G mm-wave applications using slot characteristics," *IEEE Open J. Antennas Propag.*, vol. 4, pp. 81–90, 2023.
[46] H. Wang and P. Wu, "Wideband MIMO antennas for 5G mobile terminals," *IEEE Open J. Antennas Propag.*, vol. 4, pp. 74–80, 2023.
[47] J. Kumar, B. Basu, and F. Talukdar, "Modeling of a PIN diode RF switch for reconfigurable antenna application," *Scientia Iranica*, vol. 26, no. 3, pp. 1714–1723, 2019.
[48] S. Zhu, H. Liu, P. Wen, Z. Chen, and H. Xu, "Vivaldi antenna array using defected ground structure for edge effect restraint and back radiation suppression," *IEEE Antennas Wireless Propag. Lett.*, vol. 19, pp. 84–88, 2020.

MING-AN CHUNG (Senior Member, IEEE) received the B.Eng. and M.Eng. degrees in electronic engineering from Chang Gung University, Taoyuan, Taiwan, in 2003 and 2005, respectively, and the D.Eng. degree in electrical engineering from the National Taiwan University of Science and Technology (NTUST), Taipei, Taiwan, in 2016. He is currently an Associate Professor with the Department of Electronic Engineering, National Taipei University of Technology (NTUT), where he is also the Leader of the Innovation Wireless Communication and Electromagnetic Applications Laboratory. His research interests include wireless communication propagation, intelligent robotics, self-driving vehicles, antenna design for various mobile and wireless communications, electromagnetic theory, and applications. He is also a Reviewer of many scientific journals, including IEEE TRANSACTIONS ON ANTENNAS AND PROPAGATION, IEEE TRANSACTIONS ON INDUSTRIAL INFORMATICS, *Journal of Intelligent and Robotic Systems*, *IET Microwaves, Antennas and Propagation*, IEEE ANTENNAS AND WIRELESS PROPAGATION LETTERS, *International Review of Electrical Engineering*, *International Journal on Communications Antenna and Propagation*, and *AEÜ-International Journal of Electronics and Communications*, and many international conferences, including ICRA, ICCE-TW, RFIT, ICBEB, EMCAR, and SNSP.

CHIA-WEI LIN received the B.S. and M.S. degrees from Chung Yuan Christian University, in 2007. He is currently pursuing the Ph.D. degree in electrical engineering with the National Taipei University of Technology. His research interests include wireless communication propagation research, antenna design, intelligent robotics research, self-driving vehicle research, embedded systems, and deep learning.

CHIH-WEI YANG received the B.S. degree from the St. John's University of Technology, in 2016. He is currently pursuing the M.S. degree in electronic engineering with the National Taipei University of Technology. His research interests include high-frequency device research, near-field communication research, and RFIC design research.

ING-PENG MEIY received the master's degree in electronic engineering from the National Taipei University of Technology, in 2023. His current research interests include millimeter-wave and sub-terahertz antenna research, chip filter research, and other RFIC component research.